CrossMark

# Investigation of NiO$_x$-hole transport layers in triple cation perovskite solar cells

Stefan Weber[1] · Thomas Rath[1] · Jimmy Mangalam[1] · Birgit Kunert[2] · Anna Maria Coclite[2] · Martin Bauch[3] · Theodoros Dimopoulos[3] · Gregor Trimmel[1]

## Abstract

Perovskite solar cells with a planar p-i-n device structure offer easy processability at low temperatures, suitable for roll-to-roll fabrication on flexible substrates. Herein we investigate different hole transport layers (solution processed NiO$_x$, sputtered NiO$_x$, PEDOT:PSS) in planar p-i-n perovskite solar cells using the triple cation lead halide perovskite Cs$_{0.08}$(MA$_{0.17}$FA$_{0.83}$)$_{0.92}$Pb(I$_{0.83}$Br$_{0.17}$)$_3$ as absorber layer. Overall, reproducible solar cell performances with power conversion efficiencies up to 12.8% were obtained using solution processed NiO$_x$ as hole transport layer in the devices. Compared to that, devices with PEDOT:PSS as hole transport layer yield efficiencies of approx. 8.4%. Further improvement of the fill factor was achieved by the use of an additional zinc oxide nanoparticle layer between the PC$_{60}$BM film and the Ag electrode.

## 1 Introduction

The investigation of inorganic–organic hybrid perovskite solar cells is of major interest since its massive increase in power conversion efficiency (PCE) from 3.8% [1] in 2009 to 22.1% in 2016 [2]. The highest PCEs so far were achieved in n-i-p device architectures, using mesoporous TiO$_2$ as electron transport layer (ETL) and spiro-OMeTAD as hole transport layer (HTL), respectively [3]. Recently, Saliba et al. introduced a triple cation perovskite, using a combination of methylammonium, formamidinium and cesium ions (MA/FA/Cs) and a mixture of bromide and iodide reaching PCE values of more than 20% together with enhanced device stability. Maximum PCEs of 21.1% and 20.96% were reached with a Cs$_x$(MA$_{0.17}$FA$_{0.83}$)$_{(100-x)}$Pb(I$_{0.83}$Br$_{0.17}$)$_3$ perovskite absorber layer where x = 5 and 10, respectively. This A-site cation combination results in the suppression of the photovoltaic non-active "yellow phase" and enhances perovskite crystallinity. However, so far this route is mainly investigated in n-i-p based perovskite solar cells [4–6]. In these structures, TiO$_2$ is used as ETL in most cases in combination with HTLs such as spiro-OMeTAD or other organic HTLs [7]. Despite reaching high efficiencies, commonly high temperature processing is required for the preparation of the compact and mesoporous TiO$_2$ films limiting low cost and energy efficient fabrication. Compared to the n-i-p device structures containing mesoporous TiO$_2$, p-i-n planar devices offer low temperature fabrication, which is favourable for roll-to-roll fabrication [8, 9]. In p-i-n perovskite devices, usually PCBM is used as ETL and poly(3,4-ethylenedioxythiophene) polystyrene sulfonate (PEDOT:PSS) as HTL. However, due to its acidic nature and hygroscopic character, devices with PEDOT:PSS layers might degrade faster than devices with e.g. NiO$_x$ hole transport layers, which have a similar valence band energy as PEDOT:PSS films [10–14]. Some research groups also reported better crystallinity of the perovskite film on a NiO$_x$ layer than on PEDOT:PSS [15, 16]. NiO$_x$ is an inorganic metal oxide semiconductor, which exhibits high optical transmittance, high stability, easy processability, and a wide band gap that allows high hole mobility and good electron blocking ability [17, 18]. There exist several methods for NiO$_x$ deposition, like atomic layer deposition, flame spray synthesis, pulsed laser deposition, sputtering and electrodeposition [16, 19–22]. However, for fast and large scale roll-to-roll fabrication, coating or printing processes for the application of the NiO$_x$ films are of interest. In this regard,

✉ Thomas Rath
thomas.rath@tugraz.at

1 Institute for Chemistry and Technology of Materials (ICTM), NAWI Graz, Graz University of Technology, Stremayrgasse 9, 8010 Graz, Austria

2 Institute of Solid State Physics, NAWI Graz, Graz University of Technology, Petersgasse 16, 8010 Graz, Austria

3 AIT Austrian Institute of Technology, Center for Energy, Photovoltaic Systems, Giefinggasse 2, 1210 Vienna, Austria

several methods using spin coating followed by an additional annealing step are reported [23–25]. Interestingly, higher temperature treatment of the $NiO_x$ films significantly affects the device performance. Jiang et al. reported that annealing $NiO_x$ above 150 °C reduces the device performance due to the formation of $Ni_2O_3$ species [26]. A reduction of the device performance was also seen by Hou et al. when heating the $NiO_x$ film above 140 °C [16]. Moreover, it was shown that p-i-n devices with $MAPbI_3$ as absorber layer reveal low to almost negligible hysteresis, especially if $NiO_x$ is used as HTL [9, 27]. Recently, a PCE of 18.4% for perovskite-based solar cells with a $NiO_x$ HTL was reported by Bai et al. who investigated the perovskite crystal growth on $NiO_x$ films and the formation of intermediate layers ($MAPbI_3$-DMSO) with increasing DMSO concentration [25].

In this work, we investigate and compare different hole transport layers (HTLs), namely solution based $NiO_x$, sputtered $NiO_x$, and PEDOT:PSS, in solar cells using the triple cation lead halide perovskite $Cs_{0.08}(MA_{0.17}FA_{0.83})_{0.92}Pb(I_{0.83}Br_{0.17})_3$ as absorber layer in terms of solar cell performance and hysteresis properties of the devices.

## 2 Results and discussion

### 2.1 Preparation and characterisation of the hole transport layers

The synthesis of the $NiO_x$ nanoparticles was adapted from literature [9, 26, 27] and is conducted at room temperature with a subsequent drying step at 80 °C and a temperature

treatment at 270 °C, which results in non-stoichiometric $NiO_x$ [26, 27]. The X-ray diffraction pattern in Fig. 1a, shows five distinct reflections at 37.2°, 43.3°, 62.7°, 75.4° and 79.4° 2θ which correspond to the lattice planes (111), (200), (220), (311), and (222) of $NiO_x$ in the cubic crystal structure [27]. It also indicates that neither $Ni(OH)_2$ nor $NaNO_3$ impurities are present. The primary crystallite size was estimated using the Scherrer equation to be around 8 nm.

To prepare $NiO_x$ thin films, the nanoparticles were dispersed in deionized water to form a black ink, which was used for spin coating in ambient conditions. After spin casting, the $NiO_x$ layers did not undergo further annealing or post-treatment steps. The layer thickness was found to be between 29 and 39 nm. Alternatively, 10 nm thick $NiO_x$ layers were prepared by sputtering. The $NiO_x$ layers were sputtered from an oxide target (4-in. in diameter) using a RF magnetron source at a power of 200 W in an $Ar/O_2$ (80/20) mixture and a gas pressure of 5 μbar [28]. PEDOT:PSS layers (~ 35 nm) were prepared by spin coating.

In Fig. 2a, the transmission spectra of the investigated HTLs are shown. The solution processed $NiO_x$ nanoparticle film as well as the PEDOT:PSS film showed high transparency greater than 80% on indium tin oxide (ITO) substrates. Compared to that, the sputtered $NiO_x$ film showed less transmission of around 70%. In sputtering experiments with different $Ar/O_2$ ratios, we found that a higher $O_2$ content (up to 20%) fosters the formation of films with higher transparency. Based on that we assume that the diminished transmission stems most likely from low oxygen content in the sputtered $NiO_x$ films. We increased the transmittance of the sputtered $NiO_x$ films by an annealing step at 150 °C in ambient
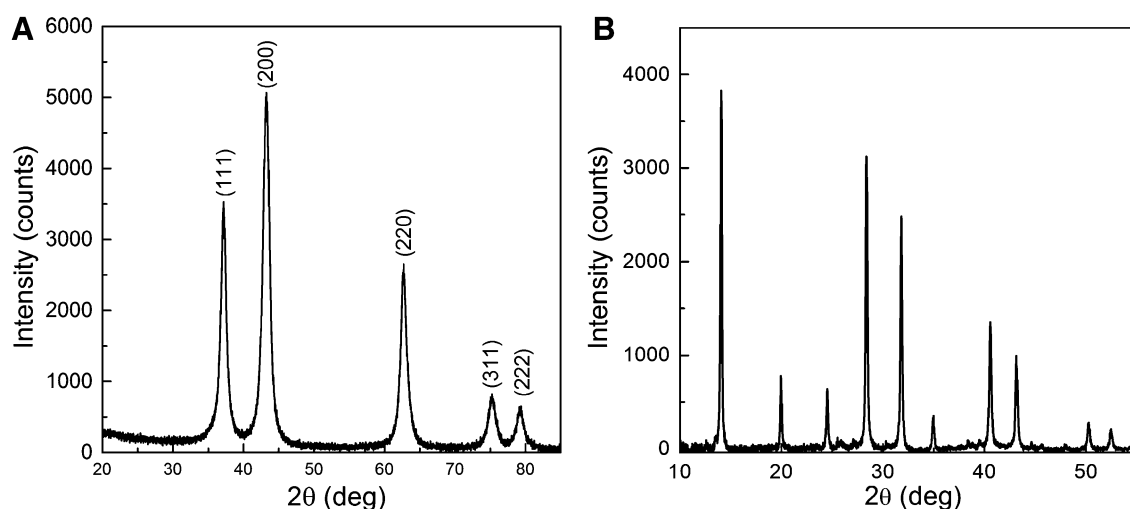


**Fig. 1** X-ray diffractogram of the $NiO_x$ nanocrystals displaying the reflections of cubic $NiO_x$ at 37.2°, 43.3°, 62.7°, 75.4° and 79.4° 2θ, which match well with the reference PDF 01-078-0429 (**a**); X-ray diffractogram of the $Cs_{0.08}(MA_{0.17}FA_{0.83})_{0.92}Pb(I_{0.83}Br_{0.17})_3$ perovskite on a glass substrate displaying all characteristic reflections according to Ref. [7] (**b**)
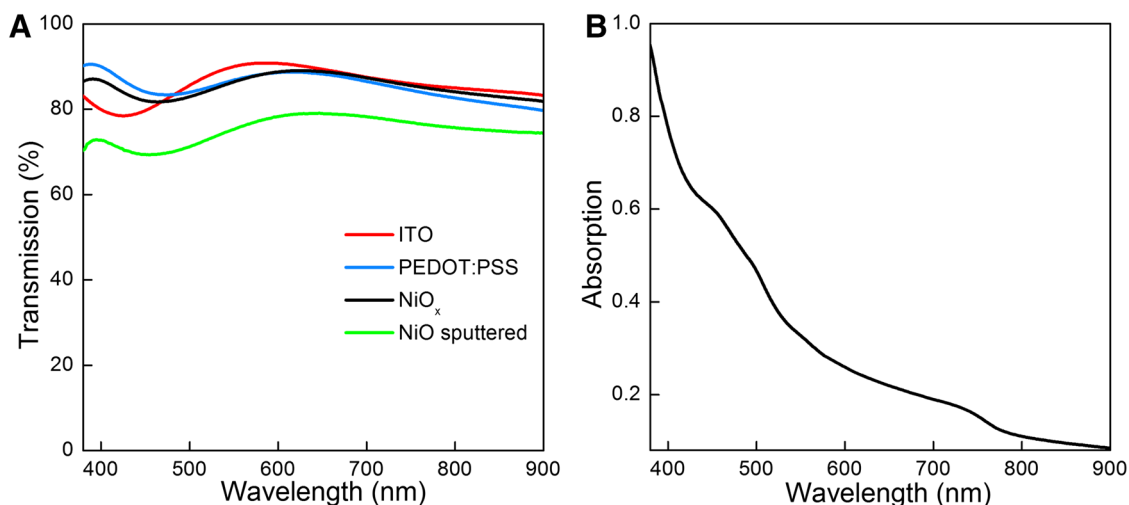
**Fig. 2 a** Transmission spectra of glass substrates covered with ITO, ITO/solution processed $NiO_x$, ITO/sputtered $NiO_x$ and ITO/PEDOT:PSS; **b** Absorption spectrum of the $Cs_{0.08}(MA_{0.17}FA_{0.83})_{0.92}Pb(I_{0.83}Br_{0.17})_3$ perovskite on a glass substrate. The precursor solution was 1:4 diluted compared to the precursor used for solar cell fabrication [solvent: DMF:DMSO (1:4 v/v)]

conditions, however, in this case problems with the wettability of the perovskite coating solution and consequently with the homogeneity of the perovskite layers occurred. Consequently, non-annealed sputtered $NiO_x$ films were used for further experiments.

## 2.2 Preparation of the triple cation perovskite— $Cs_{0.08}(MA_{0.17}FA_{0.83})_{0.92}Pb(I_{0.83}Br_{0.17})_3$

The triple cation perovskite approach incorporating cesium (Cs), methylammonium (MA), and formamidinium (FA) as monovalent cations was adopted from Saliba et al. [7] and was prepared with a Cs-content of 8% (see Sect. 4). By combining these three different cations (MA/FA/Cs), the mixed cation perovskite crystalizes in a cubic crystal structure, which corresponds to a black phase [4]. In Fig. 1b, the X-ray diffractogram of the triple cation perovskite (prepared on a glass substrate) shows the typical pattern of the perovskite structure and matches well with literature data [7]. As can be further seen, no impurities such as lead iodide, methylammonium iodide or $FAPbI_3$ were observed. The addition of Cs fosters the formation of the desired black phase and suppresses the yellow phase of $FAPbI_3$ [4]. Another important issue is the ratio of the solvent mixture to obtain a uniform film formation. Herein a mixture of DMSO/DMF (4/1 v/v) was used because the strong coordinative solvent DMSO enhances the dissolution of $PbI_2$ [29]. The perovskite film thicknesses were in the same range (280–320 nm) on all substrates and interfacial layers. The surface morphology of a perovskite film prepared on a glass/ITO/$NiO_x$ substrate was investigated by SEM and can be seen in Fig. 3a. The top view image indicates homogenous growth on $NiO_x$ with

complete coverage of the perovskite film without obvious pinholes and grain sizes ranging from ~100 to 500 nm. The absorption spectrum (shown in Fig. 2b) corresponds to the data in the literature [4, 6].

## 2.3 Device preparation

Up to now, Cs—containing mixed ion perovskite solar cells were mostly fabricated in n-i-p device structures on mesoporous $TiO_2$ [4, 6]. In our study, this efficient perovskite absorber is investigated in the planar p-i-n structure adopted from organic solar cells, which already gave promising PCE values with $MAPbI_3$ absorber layers ranging from 10% to above 18% [8, 17, 19, 25, 27, 30]. A scheme of the used solar cell architecture is depicted in Fig. 3b. In a first step, the respective HTL is deposited on glass/ITO substrates. Subsequently, the perovskite absorber layer is coated, followed by the deposition of a 50 nm thick $PC_{60}BM$ layer as ETL. The solar cells were completed by the deposition of silver electrodes with a thickness of approximately 120 nm by thermal evaporation. In Fig. 3c, an energy level diagram of the used materials in the solar cells is presented. Compared to PEDOT:PSS (valence band of −5.2 eV), the valence band (VB) of $NiO_x$ (−5.49 eV) is well aligned to the VB of the mixed cation perovskite (−5.50 eV). $NiO_x$ exhibits a high conduction band (CB) of −1.85 eV whereas the CB of the perovskite is only −3.88 eV, which makes $NiO_x$ a good electron blocking layer [6, 9, 26, 31]. $PC_{60}BM$ (CB: −4.2 eV) acts as electron transport layer in this device configuration [14, 32].

In Fig. 4 cross sectional SEM images of the prepared solar cells are displayed. In the images of the devices with
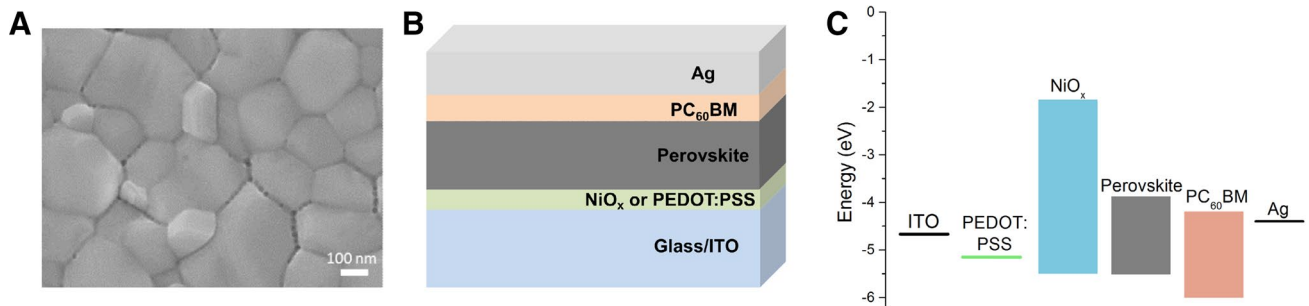
**Fig. 3** Top view SEM image of a perovskite film prepared on a NiO$_x$ layer (**a**), a schematic representation of the device structure (p-i-n type) used in this study (**b**), and the corresponding energy level diagram: ITO ($-4.7$ eV) [26], NiO$_x$ ($-5.49$ to $-1.85$ eV) [26], PEDOT:PSS ($-5.2$ eV) [31], triple cation perovskite ($-5.5$ to $-3.88$ eV) [6], PC$_{60}$BM ($-6.0$ to $-4.2$ eV) [14, 32] and silver (Ag) ($-4.4$ eV) [22]

a solution processed NiO$_x$ HTL depicted in Fig. 4a, d, the NiO$_x$ nanoparticle films can be clearly seen and the distribution appears inhomogeneous. However, this inhomogeneity most likely does not stem from the spin coating process, but from breaking the device for the analysis of the cross-section. For the devices with PEDOT:PSS hole transport layer (Fig. 4b, e) a homogenous PEDOT:PSS film with a thickness of around 35 nm was observed. Also the sputtered NiO$_x$ layer appears very homogenous in the cross sectional SEM images in Fig. 4c, f and the thickness is approx. 10 nm. In the cross sections of all devices, the perovskite films reveal a thickness between 280 and 320 nm. On top of the perovskite films, the PC$_{60}$BM layers, which appear slightly darker, can be distinguished and the devices in (Fig. 4d–f) are prepared with an additional ZnO nanoparticle layer. The ZnO nanoparticle film is homogenous in all samples, covering the PC$_{60}$BM film with a layer thickness of around 70–100 nm.

In a next step, the film thickness of the solution processed NiO$_x$ layer was varied and its influence on the solar cell performance was studied. By changing the spin coating parameters, NiO$_x$ layers with thicknesses of 29, 34 and 39 nm ($\pm 1$ nm) were deposited. Figure 5a shows the
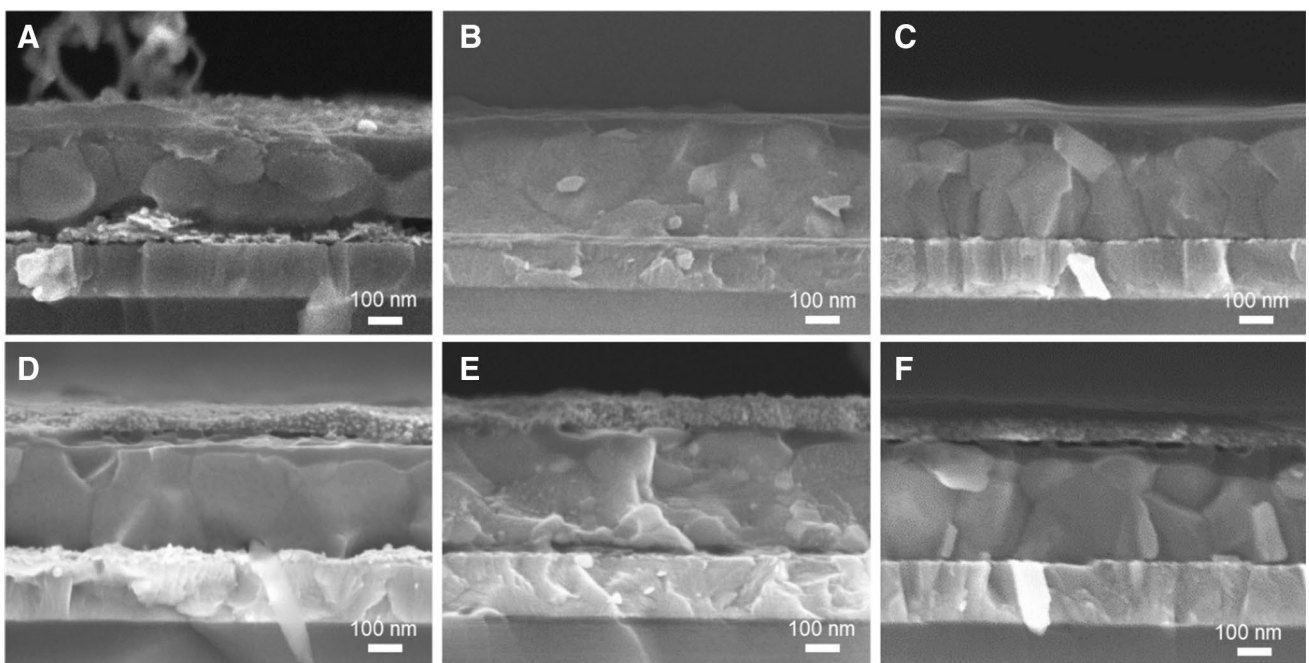


**Fig. 4** Cross sectional SEM images acquired using an in-lens detector of solar cells with a solution processed NiO$_x$ HTL (**a**), a PEDOT:PSS HTL (**b**), a sputtered NiO$_x$ HTL (**c**), a solution processed NiO$_x$ HTL with an additional ZnO interfacial layer between the PC$_{60}$BM layer and the Ag electrode (**d**), a PEDOT:PSS HTL with a ZnO interfacial layer (**e**), and with a sputtered NiO$_x$ HTL with a ZnO interfacial layer (**f**)

current density–voltage (J–V) curves of typical devices. Table 1 summarizes the characteristic J–V parameters of these cells. Solar cells with $NiO_x$ layers of 29 and 34 nm exhibit very similar device parameters, with $V_{OC}$ values about 0.95 V, $J_{SC}$ values about 22 mA/cm$^2$ and FF values about 60% yielding overall PCEs of approx. 13%. In contrast to that, for solar cells with $NiO_x$ layers of 39 nm, the $J_{SC}$ values are reduced to about 19 mA/cm$^2$ and the FF to values of 53% yielding to typical PCEs values of 9%. The doubling of the series resistance indicates that the $NiO_x$-layer is getting too thick. Other important aspects which have to be taken into account are voids or pinholes that increase in number when the layer thickness of $NiO_x$ is decreased [33]. This is consistent with our findings. The shunt resistance is getting higher with increasing layer thickness. In this regard, the solar cells with 34 nm thick $NiO_x$ films showing the highest FF and good $V_{OC}$ and $J_{SC}$ values have been chosen for further optimization. Moreover, the devices are showing only a small hysteresis as can be seen exemplarily in Fig. 5b.

Next, solar cells with sputtered $NiO_x$ (10 nm) and PEDOT:PSS as HTL and devices without HTL have been investigated. In Fig. 5b, the J–V curves of the best devices are compared with those of solar cells using solution processed $NiO_x$ (34 nm). The corresponding device parameters

of these solar cells as well as the mean values and the standard deviations are given in Table 2. Compared to the solar cells with the solution processed $NiO_x$ HTL, in devices with a sputtered $NiO_x$ film, the PCE was reduced from 12.6 to 8.3%, which is mainly due to a significantly lower FF. The reason for the lower FF (51%) is most likely the low film thickness of the sputtered $NiO_x$ film of only 10 nm and thereby insufficient electron blocking properties. With the sputtered $NiO_x$ layers, a trade-off needs to be made. On one hand, for thicker $NiO_x$ layers, the shunt resistance and electron blocking properties are better, but the series resistance and the absorption losses are high. On the other hand, for thin $NiO_x$ layers, the absorption losses are moderate but the shunt resistance and electron blocking properties suffer (see Table 2). The high optical losses are maybe the most critical factor here, which does not come into play for the nanoparticle-based $NiO_x$ layer.

The prepared devices with PEDOT:PSS as HTL show a lower $V_{OC}$ (0.74 V) compared to $NiO_x$-based devices (0.91–0.94 V). As was found by Liu et al., this lower $V_{OC}$ is most likely due to the fact that methylammonium iodide can decrease the intrinsic p-doping in PEDOT:PSS leading to a reduced work function and non-efficient hole collection [34].

For comparison purposes, we also prepared devices without HTL. Due to the absence of a hole selective contact,
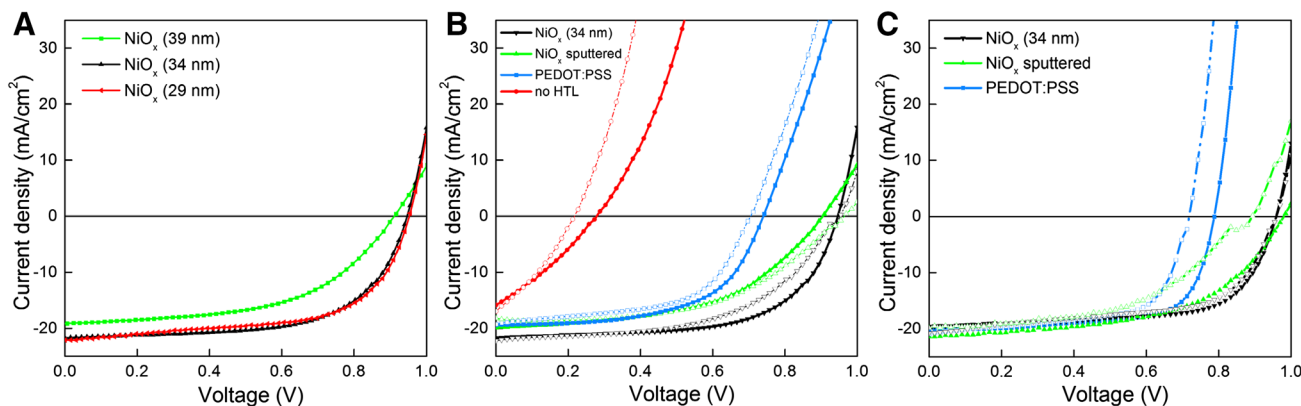


**Fig. 5** **a** J–V curves of solar cells with different layer thicknesses of the solution processed $NiO_x$ HTL; **b** typical J–V curves of solar cells prepared with solution processed $NiO_x$, sputtered $NiO_x$, PEDOT:PSS, and without HTL measured in forward and backward direction from 0 to 1 V with a scan rate of 150 mV/s; **c** J–V curves of devices with solution processed $NiO_x$, sputtered $NiO_x$ and PEDOT:PSS HTLs with an additional ZnO interfacial layer between the $PC_{60}BM$ film and the silver electrode measured in forward and backward direction from 0 to 1 V with a scan rate of 150 mV/s. The J–V curves measured in backward direction (BWD) are denoted with solid symbols, the curves measured in forward direction (FWD) with hollow symbols

**Table 1** Characteristic parameters of the solar cells prepared with different thicknesses of the solution processed $NiO_x$ HTL

| Layer thickness (nm) | $R_s$ ($\Omega$ cm$^2$) | $R_{sh}$ ($\Omega$ cm$^2$) | $V_{OC}$ (V) | $J_{SC}$ (mA/cm$^2$) | FF (%) | PCE (%) |
|---|---|---|---|---|---|---|
| 29 ± 1 | 5.0 | 303 | 0.95 | 22.1 | 61.0 | 12.7 |
| 34 ± 1 | 4.9 | 355 | 0.94 | 21.7 | 62.8 | 12.8 |
| 39 ± 1 | 10.6 | 435 | 0.92 | 19.1 | 53.2 | 9.3 |

**Table 2** Characteristic parameters of the solar cells with solution processed or sputtered $NiO_x$, PEDOT:PSS, or no HTL

| HTL | | $R_s$ ($\Omega$ cm$^2$) | $R_{sh}$ ($\Omega$ cm$^2$) | $V_{OC}$ (V) | $J_{SC}$ (mA/cm$^2$) | FF (%) | PCE (%) |
|---|---|---|---|---|---|---|---|
| $NiO_x$ NPs (34 nm) | Best cell | 4.9 | 355 | 0.94 | 21.7 | 62.8 | 12.8 (10.5[a]) |
| | Average | | | $0.96 \pm 0.03$ | $20.9 \pm 0.64$ | $63.1 \pm 1.4$ | $12.6 \pm 0.49$ |
| $NiO_x$ (sputtered) | Best cell | 11.4 | 307 | 0.91 | 19.9 | 51.0 | 9.1 |
| | Average | | | $0.88 \pm 0.02$ | $19.4 \pm 0.46$ | $49.0 \pm 1.3$ | $8.3 \pm 0.53$ |
| PEDOT:PSS | Best cell | 6.3 | 769 | 0.74 | 19.4 | 58.3 | 8.4 |
| | Average | | | $0.77 \pm 0.11$ | $19.3 \pm 1.08$ | $55.5 \pm 5.4$ | $8.2 \pm 0.40$ |
| w/o HTL | Best cell | 13.1 | 23 | 0.27 | 15.8 | 30.8 | 1.3 |
| | Average | | | $0.30 \pm 0.02$ | $15.2 \pm 0.63$ | $27.9 \pm 2.6$ | $1.3 \pm 0.06$ |

The mean values and standard deviations are calculated from the best solar cells of the respective configuration prepared in this study

[a]Illumination through a shadow mask

the $V_{OC}$ as well as the fill factor in these solar cells are significantly reduced and PCEs of only approx. 1% could be obtained.

Regarding the hysteresis behaviour, for solar cells with solution processed or sputtered $NiO_x$ HTLs low hysteresis was observed, whereas devices with PEDOT:PSS layers show a more pronounced one. When using no HTL, a strong hysteresis effect could be seen (Fig. 5b).

The J–V curves of solar cells with solution processed and sputtered $NiO_x$ as well as PEDOT:PSS HTLs and an additional ZnO nanoparticle interlayer on top of the $PC_{60}BM$ film measured in forward and backward scan direction are depicted in Fig. 5c and the corresponding device parameters are summarized in Table 3. Devices using solution processed $NiO_x$ as HTL revealed again the highest PCE of 12.6% with an average of $12.5 \pm 0.19$%. In all devices, the FF increased independent of the used HTL, which is attributed to a reduced leakage path and improved hole blocking properties of the ETL.

Moreover, by the deposition of the ZnO nanoparticle layer, the hysteresis effect was diminished even further for the solar cells prepared with a solution processed $NiO_x$ hole transport layer (see Fig. 5c). As can be also seen in Fig. 5c, the addition of the ZnO interlayer does not have a positive influence on the hysteresis behaviour of the devices with sputtered $NiO_x$ or PEDOT:PSS HTLs.

## 3 Conclusion

In conclusion, $NiO_x$ HTLs led—compared to PEDOT:PSS HTLs—to higher power conversion efficiencies of solar cells with the triple cation lead halide perovskite $Cs_{0.08}(MA_{0.17}FA_{0.83})_{0.92}Pb(I_{0.83}Br_{0.17})_3$ as absorber layer. In this study, two types of $NiO_x$ HTLs were investigated, whereby solution processed $NiO_x$ HTLs, prepared from $NiO_x$ nanoparticle inks, performed better than sputtered $NiO_x$ films. The lower PCE of the devices with a PEDOT:PSS HTL is mainly due to a decreased $V_{OC}$ and a lower FF. SEM images of the cross sections of the investigated devices revealed similar thicknesses of the perovskite absorber layer (280–320 nm) in all devices and good homogeneity of all layers in the solar cell stack.

Furthermore, compared to devices with PEDOT:PSS as HTL, solar cells with a solution processed nanoparticle based $NiO_x$ HTL showed very small hysteresis. The incorporation of a ZnO nanoparticle layer as an additional ETL between the $PC_{60}BM$ film and the silver electrode significantly improved the FF of the devices prepared with the different HTLs.

**Table 3** Performance of the solar cells with an additional ZnO interfacial layer between the $PC_{60}BM$ layer and the silver electrode

| HTL | | $R_s$ ($\Omega$ cm$^2$) | $R_{sh}$ ($\Omega$ cm$^2$) | $V_{OC}$ (V) | $J_{SC}$ (mA/cm$^2$) | FF (%) | PCE (%) |
|---|---|---|---|---|---|---|---|
| $NiO_x$ NPs (34 nm) | Best cell | 4.4 | 469 | 0.95 | 19.6 | 66.9 | 12.6 (11.7[a]) |
| | Average | | | $0.98 \pm 0.02$ | $19.6 \pm 0.33$ | $65.1 \pm 1.4$ | $12.5 \pm 0.19$ |
| $NiO_x$ sputtered | Best cell | 8.9 | 317 | 0.98 | 21.3 | 54.1 | 11.3 |
| | Average | | | $0.99 \pm 0.01$ | $21.0 \pm 0.50$ | $52.1 \pm 1.3$ | $10.8 \pm 0.32$ |
| PEDOT:PSS | Best cell | 2.8 | 309 | 0.79 | 20.3 | 68.6 | 10.9 |
| | Average | | | $0.77 \pm 0.02$ | $19.2 \pm 0.69$ | $68.0 \pm 2.2$ | $10.0 \pm 0.66$ |

[a]Illumination through a shadow mask

# 4 Experimental details

## 4.1 Materials

All chemicals and solvents were used as purchased without any further purification. Nickel(II) nitrate hexahydrate was purchased from Fluka, sodium hydroxide (NaOH) from VWR, lead iodide ($PbI_2$) from TCI, poly(3,4-ethylenedioxythiophene) polystyrene sulfonate (PEDOT:PSS)—P VP AI 4083 from Heraeus, lead bromide ($PbBr_2$) and dimethylsulfoxide (DMSO) from Alfa Aesar, [6,6]-Phenyl $C_{61}$ butyric acid methyl ester ($PC_{60}BM$) from Solenne, and silver from Kurt J. Lesker Company. All the other chemicals were purchased from Sigma Aldrich.

## 4.2 Preparation of ITO substrates

Patterned glass/ITO substrates ($15 \times 15 \times 1.1$ mm) ($10 \Omega$/sq) from Xinyan Technology were pre-cleaned with acetone, put in an isopropyl alcohol bath and placed in an ultrasonic bath at 40 °C for 30 min. The substrates were then dried with $N_2$ and further plasma etched for 3 min.

## 4.3 $NiO_x$ nanoparticle synthesis and film formation

The nickel(II) oxide nanoparticles were synthesized according to literature with small changes [9, 26, 27]. Briefly, nickel(II) nitrate hexahydrate ($NiNO_3 \cdot 6H_2O$) (0.05 mol) was dispersed in 10 ml deionized water and stirred for 5 min. Afterwards sodium hydroxide (NaOH, 10 M) was added dropwise to adjust a pH of 10, which results in a colour change from dark to light green. The colloidal precipitate was then washed with deionized water to remove side products. The light green residue was then dried at 80 °C for 6 h and further calcinated at 270 °C for 2 h, resulting in non-stoichiometric black nickel(II) oxide nanoparticles. In a next step, the $NiO_x$ NPs (2 wt%) were dispersed in deionized water, placed in an ultrasonic bath at 40 °C for 2 h and filtered through a 0.45 µm PVDF syringe filter to produce the $NiO_x$ ink used for thin film formation. The $NiO_x$ nanoparticle ink was spin coated at different speeds (2500–4500 rpm) for 30 s and the $NiO_x$ films on the glass/ITO substrates were dried at room temperature for 1 h.

## 4.4 PEDOT:PSS film formation

PEDOT:PSS (P VP AI 4083) (0.5 ml) was mixed with 1 ml isopropyl alcohol, placed in an ultrasonic bath for 1 h and filtered through a 0.45 µm PVDF syringe filter. The solution was then spin coated in ambient air at 3000 rpm for 60 s followed by drying at 130 °C for 20 min also in ambient air. Afterwards, to increase the wettability of the perovskite solution, the substrates were treated with isopropyl alcohol by placing the substrate on a spin coater, applying 200 µl of isopropyl alcohol on the PEDOT:PSS film followed by a spin coating step (2000 rpm for 2 s, 4000 rpm for 10 s) to dry the substrate and an additional annealing step with the same parameters as used before (130 °C for 20 min) [30].

## 4.5 Sputtered $NiO_x$

The 4-in. diameter $NiO_x$ target was mounted on a RF magnetron source and sputtered at 200 W in $Ar/O_2$ (80/20) atmosphere, at a pressure of 5 µbar, without substrate heating. The sputtering tool was a Leybold Univex 450C with a base vacuum of $1 \times 10^{-7}$ mbar.

## 4.6 Perovskite precursor and film formation

The triple cation perovskite precursor was prepared by introducing slight changes in the procedure used by Saliba et al. [7]. The precursor consisted of lead iodide ($PbI_2$, 1.1 M), lead bromide ($PbBr_2$, 0.2 M), formamidinium iodide (FAI, 1M), and methylammonium bromide (MABr, 0.2 M) dissolved in a 1:4 (v/v) DMF:DMSO solvent mixture. A second solution of cesium iodide (CsI, 1.5 M) in DMSO was prepared and added to the first solution to get the desired Cs content of 8%. The spin coating was carried out in a two-step process at 1000 rpm for 10 s and 6000 rpm for 20 s. The spinning substrate was treated with 50 µl chlorobenzene as an anti-solvent during the last 5 s of the spinning process, which allowed the precipitation of the perovskite. The substrates were then annealed at 100 °C for 1 h. All steps were carried out inside a glovebox with nitrogen atmosphere.

## 4.7 Electron transport layer film formation and top electrode

A 20 mg/ml solution of $PC_{60}BM$ in chlorobenzene was prepared and stirred for 2 h at room temperature under nitrogen atmosphere [27]. The solution was spin coated at 2000 rpm for 60 s. Afterwards, the top electrode (120 nm Ag) was deposited by thermal evaporation under high vacuum conditions ($1 \times 10^{-5}$ mbar) using a shadow mask (active area of 0.09 $cm^2$).

## 4.8 Interfacial layer film formation

A zinc oxide nanoparticle ink (purchased from Sigma Aldrich) was spin coated on the $PC_{60}BM$ layer at 3000 rpm

for 30 s without any further treatment under nitrogen atmosphere before the deposition of the silver electrode.

## 4.9 Characterization

The NiO$_x$ nanoparticles as well as the triple cation perovskite were characterized by X-ray diffraction with a PANalytical Empyrean system which uses Cu K alpha radiation. UV–Vis measurements of the HTLs were performed using the UV/VIS Spectrometer—Lambda 35 by Perkin Elmer. The layer thicknesses of all HTLs were determined by ellipsometry using a M-2000 instrument (J.A. Woollam Co., USA) in reflection at incident angles of 65°, 70° and 75°. The optical data were recorded in the wavelength range of 370–1000 nm. The experimental data were modeled with the CompleteEASE® software, using a three-layer system consisting of the silicon substrate, the interfacial oxide layer and a Cauchy function with Urbach tail as top layer.

The thicknesses of the absorber material and the ETLs were measured by surface profilometry using a DektakXT device by Bruker as well as by cross sectional SEM images acquired on a Zeiss-Supra 40 scanning electron microscope with an in-lens detector.

J–V curves of all devices were measured inside a glove box (nitrogen atmosphere) with a scan rate of 150 mV/s using a Keithley 2400 source meter connected to a LabView-based software. The light with an irradiation of 100 mW/cm$^2$ was produced by a Dedolight DLH400 lamp, which was calibrated using a pyranometer from Kipp & Zonen.

## References

1. A. Kojima, K. Teshima, Y. Shirai, T. Miyasaka, J. Am. Chem. Soc. **131**, 6050 (2009)
2. M.A. Green, Y. Hishikawa, W. Warta, E.D. Dunlop, D.H. Levi, J. Hohl-Ebinger, A.W.H. Ho-Baillie, Prog. Photovolt. **25**, 668 (2017)
3. S. Yang, W. Fu, Z. Zhang, H. Chen, C.-Z. Li, J. Mater. Chem. A **5**, 11462 (2017)
4. J.-P. Correa-Baena, A. Abate, M. Saliba, W. Tress, T.J. Jacobsson, M. Grätzel, A. Hagfeldt, Energy Environ. Sci. **10**, 710 (2017)
5. M. Saliba, T. Matsui, K. Domanski, J.-Y. Seo, A. Ummadisingu, S.M. Zakeeruddin, J.-P. Correa-Baena, W.R. Tress, A. Abate, A. Hagfeldt, M. Grätzel, Science **354**, 206 (2016)
6. M. Deepa, M. Salado, L. Calio, S. Kazim, S.M. Shivaprasad, S. Ahmad, Phys. Chem. Chem. Phys. **19**, 4069 (2017)
7. M. Saliba, T. Matsui, J.-Y. Seo, K. Domanski, J.-P. Correa-Baena, M.K. Nazeeruddin, S.M. Zakeeruddin, W. Tress, A. Abate, A. Hagfeldt, M. Grätzel, Energy Environ. Sci. **9**, 1989 (2016)
8. J. Ciro, R. Betancur, S. Mesa, F. Jaramillo, Sol. Energy Mater. Sol. Cells **163**, 38 (2017)
9. H. Zhang, J. Cheng, F. Lin, H. He, J. Mao, K.S. Wong, A.K.-Y. Jen, W.C.H. Choy, ACS Nano **10**, 1503 (2016)
10. M.P. de Jong, L.J. van IJzendoorn, M.J.A. de Voigt, Appl. Phys. Lett. **77**, 2255 (2000)
11. K. Kawano, R. Pacios, D. Poplavskyy, J. Nelson, D.D.C. Bradley, J.R. Durrant, Sol. Energy Mater. Sol. Cells **90**, 3520 (2006)
12. R. Betancur, M. Maymó, X. Elias, L.T. Vuong, J. Martorell, Sol. Energy Mater. Sol. Cells **95**, 735 (2011)
13. M.B. Islam, M. Yanagida, Y. Shirai, Y. Nabetani, K. Miyano, ACS Omega **2**, 2291 (2017)
14. U. Kwon, B.-G. Kim, D.C. Nguyen, J.-H. Park, N.Y. Ha, S.-J. Kim, S.H. Ko, S. Lee, D. Lee, H.J. Park, Sci. Rep. **6**, 30759 (2016)
15. J. You, L. Meng, T.-B. Song, T.-F. Guo, Y.M. Yang, W.-H. Chang, Z. Hong, H. Chen, H. Zhou, Q. Chen, Y. Liu, N. De Marco, Y. Yang, Nat. Nanotechnol. **11**, 75 (2016)
16. Y. Hou, W. Chen, D. Baran, T. Stubhan, N.A. Luechinger, B. Hartmeier, M. Richter, J. Min, S. Chen, C.O.R. Quiroz, N. Li, H. Zhang, T. Heumueller, G.J. Matt, A. Osvet, K. Forberich, Z.-G. Zhang, Y. Li, B. Winter, P. Schweizer, E. Spiecker, C.J. Brabec, Adv. Mater. **28**, 5112 (2016)
17. X. Yin, Z. Yao, Q. Luo, X. Dai, Y. Zhou, Y. Zhang, S. Luo, J. Li, N. Wang, H. Lin, ACS Appl. Mater. Interfaces **9**, 2439 (2017)
18. K.-C. Wang, J.-Y. Jeng, P.-S. Shen, Y.-C. Chang, E.W.-G. Diau, C.-H. Tsai, T.-Y. Chao, H.-C. Hsu, P.-Y. Lin, P. Chen, T.-F. Guo, T.-C. Wen, Sci. Rep. **4**, 4756 (2014)
19. J.H. Park, J. Seo, S. Park, S.S. Shin, Y.C. Kim, N.J. Jeon, H.-W. Shin, T.K. Ahn, J.H. Noh, S.C. Yoon, C.S. Hwang, S.I. Seok, Adv. Mater. **27**, 4013 (2015)
20. K.-C. Wang, P.-S. Shen, M.-H. Li, S. Chen, M.-W. Lin, P. Chen, T.-F. Guo, ACS Appl. Mater. Interfaces **6**, 11851 (2014)
21. A.S. Subbiah, A. Halder, S. Ghosh, N. Mahuli, G. Hodes, S.K. Sarkar, J. Phys. Chem. Lett. **5**, 1748 (2014)
22. S. Seo, I.J. Park, M. Kim, S. Lee, C. Bae, H.S. Jung, N.-G. Park, J.Y. Kim, H. Shin, Nanoscale **8**, 11403 (2016)
23. X. Yin, J. Liu, J. Ma, C. Zhang, P. Chen, M. Que, Y. Yang, W. Que, C. Niu, J. Shao, J. Power Sources **329**, 398 (2016)
24. Y. Bai, H. Chen, S. Xiao, Q. Xue, T. Zhang, Z. Zhu, Q. Li, C. Hu, Y. Yang, Z. Hu, F. Huang, K.S. Wong, H.-L. Yip, S. Yang, Adv. Funct. Mater. **26**, 2950 (2016)
25. Y. Bai, S. Xiao, C. Hu, T. Zhang, X. Meng, Q. Li, Y. Yang, K.S. Wong, H. Chen, S. Yang, Nano Energy **34**, 58 (2017)
26. F. Jiang, W.C.H. Choy, X. Li, D. Zhang, J. Cheng, Adv. Mater. **27**, 2930 (2015)
27. X. Yin, P. Chen, M. Que, Y. Xing, W. Que, C. Niu, J. Shao, ACS Nano **10**, 3630 (2016)
28. T. Dimopoulos, A. Peic, P. Müllner, M. Neuschitzer, R. Resel, S. Abermann, M. Postl, E.J.W. List, S. Yakunin, W. Heiss, H. Brückl, J. Renew. Sustain. Energy **5**, 011205 (2013)
29. Y. Wu, A. Islam, X. Yang, C. Qin, J. Liu, K. Zhang, W. Peng, L. Han, Energy Environ. Sci. **7**, 2934 (2014)
30. G. Adam, M. Kaltenbrunner, E.D. Glowacki, D.H. Apaydin, M.S. White, H. Heilbrunner, S. Tombe, P. Stadler, B. Ernecker, C.W. Klampfl, N.S. Sariciftci, M.C. Scharber, Sol. Energy Mater. Sol. Cells **157**, 318 (2016)

31. V. Shrotriya, G. Li, Y. Yao, C.-W. Chu, Y. Yang, Appl. Phys. Lett. **88**, 073508 (2006)
32. J. Cui, H. Yuan, J. Li, X. Xu, Y. Shen, H. Lin, M. Wang, Sci. Technol. Adv. Mater. **16**, 036004 (2015)
33. L. Hu, J. Peng, W. Wang, Z. Xia, J. Yuan, J. Lu, X. Huang, W. Ma, H. Song, W. Chen, Y.-B. Cheng, J. Tang, ACS Photonics **1**, 547 (2014)
34. T. Liu, F. Jiang, F. Qin, W. Meng, Y. Jiang, S. Xiong, J. Tong, Z. Li, Y. Liu, Y. Zhou, ACS Appl. Mater. Interfaces **8**, 33899 (2016)